Thermoelectric properties of pseudobrookite-based ceramics prepared from natural Fe-Ti-rich heavy mineral sand concentrate

Nina Daneu, Tina Radošević, Slavko Bernik, Darko Hanžel, Matjaž Mazaj, Marjeta Maček Kržmanc, Dejan Verhovšek, Andraž Kocjan, Mirijam Vrabec, Matjaž Spreitzer, et al.

Thermoelectric properties of pseudobrookite-based ceramics prepared from natural Fe-Ti-rich heavy mineral sand concentrate

Nina Daneu,[1*] Tina Radošević,[1,2] Slavko Bernik,[2] Darko Hanžel,[3] Matjaž Mazaj,[4] Marjeta Maček Kržmanc,[1] Dejan Verhovšek,[5] Andraž Kocjan,[2] Mirijam Vrabec,[6] Matjaž Spreitzer,[1] Emmanuel Guilmeau[7]

* Corresponding author: nina.daneu@ijs.si

[1] Advanced Materials, Jožef Stefan Institute, Jamova cesta 39, Ljubljana, Slovenia

[2] Nanostructured Materials, Jožef Stefan Institute, Jamova cesta 39, Ljubljana, Slovenia

[3] Low and Medium Energy Physics, Jožef Stefan Institute, Jamova cesta 39, Ljubljana, Slovenia

[4] Materials Chemistry, National Institute of Chemistry, Hajdrihova 19, Ljubljana, Slovenia

[5] Cinkarna Celje, d.d. Inc., Kidričeva 26, SI-3001 Celje, Slovenia

[6] Department of Geology, University of Ljubljana, Faculty of Natural Sciences and Engineering, Aškerčeva 12, 1000 Ljubljana, Slovenia

[7] CRISMAT, CNRS, Normandie Univ, ENSICAEN, UNICAEN, 14000 Caen, France

Abstract

The potential of using natural Fe-Ti-rich heavy mineral sand, as an abundant, inexpensive, and ecologically acceptable raw material for the processing of pseudobrookite-based ceramics for thermoelectric applications is presented. The as-received raw powder was used in untreated form or after pre-oxidation at 600°C, 700°C, and 800°C for 1h in an air. The starting powders were consolidated into dense compacts via conventional solid-state sintering or spark plasma sintering. The phase composition, ferrous:ferric ratio and microstructural characteristics of the powders and sintered compacts were investigated by XRD, Mössbauer spectroscopy and SEM. The samples

with a higher fraction of pseudobrookite exhibit relatively low thermal conductivity ranging between 2 and 3 W m^{-1} K^{-1}, which is promising for practical thermoelectric applications. The Seebeck coefficient depends on the ferrous:ferric ratio and is rather low, leading to low power factor values for all the samples which will have to be improved for practical applications.

Keywords: thermoelectrics, Fe-Ti-oxides, natural raw materials, functional oxides, ecologic

1. Introduction

Waste heat energy is unavoidable in many industrial processes and could be at least partially converted into usable electricity by the installation of thermoelectric (TE) generators [Araiz et al., 2020]. Currently, the most efficient TE materials are based on lead, germanium, selenium, tellurium, and other toxic, scarce, and costly elements [Wei et al., 2020]. The development of new materials with high efficiency, and stability at high temperatures, produced from abundant, economic, ecological raw materials and, at reasonable costs, would boost the production and applications of thermoelectrics, and contribute to the reduction of our carbon footprint.

Metal oxide based ceramics are a promising group of thermoelectric materials because they fulfill many criteria for high-temperature applications [Lin et al., 2019]. Among the most studied oxide thermoelectrics are layered Na- and Ca-cobaltates [Terasaki et al., 1997; Shikano and Funahashi, 2003; Masset et al., 2000], Sr-titanates including $SrTiO_3$ and layered Ruddlesden-Popper type Sr_2TiO_4 [Ohta et al., 2007; Lee et al., 2006], doped and/or nanostructured ZnO-based compositions (Ohtaki et al., 1996; Giovanelli et al., 2018; Košir et al., 2017; Labégorre et al., 2018; Guilmeau et al., 2017) and few others. The main advantages of oxide ceramics in comparison to other

thermoelectric compounds with superior efficiency are their lower toxicity, chemical stability at higher temperatures and in oxidative atmosphere, and the possibility to prepare large amounts of materials at reasonable costs. The performance of metal oxides, *i.e.* their figure of merit *ZT* ($ZT=\frac{S^2\sigma}{\kappa}T$, where *S* is the Seebeck coefficient [μV K^{-1}], σ is the electrical conductivity [mΩ cm^{-1}], κ is the thermal conductivity [W m^{-1} K^{-1}], *T* - absolute temperature [K]) is still fairly low. In general, oxide ceramics are characterized by average thermal conductivity but can exhibit high Seebeck coefficient, which is beneficial for application in thermoelectrics. On the other hand, oxides have low electrical conductivity which is mainly related to their low carrier concentration and less covalent bonding compared to for example state-of-the-art TE chalcogenides. Strategies for increasing the electrical conductivity and carrier concentration include doping and special microstructural engineering approaches.

Recently, compounds of the ferropseudobrookite (Fpb), $FeTi_2O_5$ – pseudobrookite (Psb), Fe_2TiO_5 or Fpb-Psb solid solution series, were reported as promising thermoelectrics due to their low thermal conductivity and high Seebeck coefficient [Chen et al., 2017; Chen et al., 2018; Chen et al., 2019]. Theoretical calculations [Pakizeh and Mohammadi, 2021] indicated that $Fe_{2-x}Ti_{1+x}O_5$ (x = 0, 0.5, 1.0) phases could reach figure of merit, *ZT* around unity. Pseudobrookites crystallize in an orthorhombic crystal system (*Cmcm* space group) with neither random nor perfectly ordered Fe^{2+}, Fe^{3+} and Ti^{4+} cations at 4*c* and 8*f* sites, as shown in **Figure 1a**. In ferropseudobrookite ($FeTi_2O_5$, Fpb), most of the Fe ions are in the ferrous (divalent, Fe^{2+}) state and occupy the 4*c* site. The 8*f* sites are progressively occupied with higher amounts of Fe as the compositions approach pseudobrookite (Fe_2TiO_5, Psb) [Guo et al.,1999]. Fpb starts to form already above 585°C and is stable approximately up to 1150°C. The Fpb-Psb series is one of the three solid solution series that occur in the FeO-Fe_2O_3-TiO_2 phase diagram [Lindsley, 1991]; the other two are magnetite -

ulvöspinel (Fe_3O_4-Fe_2TiO_4) series with the spinel-type structure and ilmenite-hematite ($FeTiO_3$-Fe_2O_3) series with the corundum-type structure (Figure 1b).

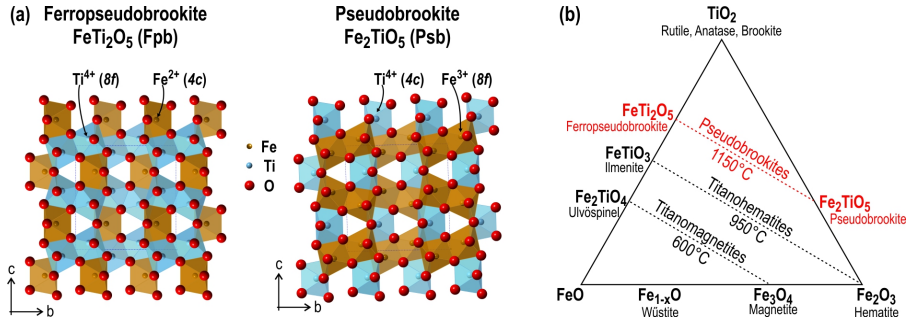

Figure 1: **(a)** Crystal structures of ferropseudobrookite ($Fe^{2+}Ti_2O_5$) and pseudobrookite ($Fe_2^{3+}TiO_5$). The Fe^{2+}, Fe^{3+} and Ti^{4+} may reside in any of the available octahedral positions (*8f* and *4c*), therefore the end-phases form a complete solid solution. **(b)** FeO-TiO_2-Fe_2O_3 phase diagram with the main phases and three solid solution series, which are stable at different temperatures.

Pseudobrookites for thermoelectric applications are usually synthesized from high-purity starting oxides (FeO, Fe_2O_3, TiO_2) by a combination of solid-state reaction and conventional pressureless solid-state sintering [Chen et al., 2017; Chen et al., 2018; Chen et al., 2019]. Natural Fe-Ti-rich powders can represent an alternative source for the preparation of pseudobrookite ceramics, especially because they are abundant and inexpensive raw materials. These powders are obtained from Fe-Ti-rich heavy mineral sands (HMS), naturally occurring concentrates of minerals with higher density. HMSs are most commonly used as a source of titanium (Ti) or titania (TiO_2) for applications in aerospace, defense, medical, pharmaceutical, food, paint, adhesive, and other industries [Jones, 2009]. The HMS accumulations form by water and wind-driven erosion

processes and the characteristic constituent minerals include ilmenite ($FeTiO_3$; ρ = 4.3-4.6 g/cm^3 depending on the alteration rate), zircon ($ZrSiO_4$; ρ = 4.6-4.7 g/cm^3), rutile (TiO_2; ρ = 4.23 g/cm^3), sillimanite (Al_2SiO_5; ρ = 3.24 g/cm^3), monazite (Ce, La, Nd, Th)PO_4, ρ = 4.8-5.5 g/cm^3), diamond (C, ρ = 3.5 g/cm^3), cassiterite (SnO_2; ρ = 6.9 g/cm^3), garnet ($X_3Y_2(SiO_4)_3$ with X = Mg, Fe, Mn, Ca and Y = Al, Fe, Cr; ρ = 3.5-4.3 g/cm^3) and others, depending on the local geological environment. The HMS is separated into different mineral phases by a combination of magnetic, electrostatic, and gravity techniques [Rejith and Mayappan, 2018]. The Fe-bearing magnetic minerals are recovered by a combination of magnetic and electrostatic separation and this fraction contains mainly ilmenite ($FeTiO_3$) possibly also some rutile and hematite. In addition, the magnetic fraction contains alteration products of ilmenite, in which Fe is partially oxidized from Fe^{2+} to Fe^{3+}. Iron may also be, to some extent, leached out of the grains to form so-called leached ilmenite ($Fe_{2+x}Ti_3O_9$), pseudorutile ($Fe_2Ti_3O_9$; $Fe_2O_3{\cdot}3TiO_2$), and leucoxene ($(Ti,Fe)_3(O)_6(OH)_6$)) [Mücke and Bhadra Chaudhuri, 1991]. Ilmenite grains occasionally contain exsolved rutile needles [Ramdohr, 1969], which are indicative of oxidation processes during the crystallization of the primary rock [Rečnik et al., 2015; Stanković et al., 2016].

In this work, we explored the possibility of preparing pseudobrookite-based ceramics for thermoelectric applications from natural Fe-Ti-rich concentrate, which is otherwise used for the extraction of TiO_2. Even though the synthesis of advanced ceramics from high-purity starting chemicals is typically recommended to avoid the effect of impurities, we show that natural Fe-Ti-rich HMS concentrate with ~95% purity is a promising raw material for the production of pseudobrookite ceramics with low thermal conductivity.

2. Experimental

2.1. Preparation of the starting powders

For our experiments, we used natural Fe-Ti-rich HMS concentrate provided by Cinkarna Metallurgical and Chemical Industry Celje, INC. The starting powder without additional treatment is the so-called as-received powder. The sand for the preparation of the concentrate originated from heavy mineral placers in Mozambique and was preliminarily milled in the Cinkarna Celje company to reach 95% of particles with a size below 40 μm for further use as raw material for the production of titania, TiO_2. The as-received powder contained around 95.4% of Fe-Ti-rich phases with 53.0 wt% of TiO_2, 23.1 wt% of Fe_2O_3, and 19.3 wt% of FeO. According to the weight fractions, the Fe:Ti atomic ratio in the as-received material was 54.4:45.6 (1.19). Detailed chemical analysis of the as-received powder is given in the Supporting Materials (**Table S1**). Three additional starting powders were prepared by pre-oxidation of the as-received powder at 600°C, 700°C and 800°C for 1 hour in an air atmosphere. Pre-oxidation of ilmenite is usually applied for increased and more efficient extraction of TiO_2 from the raw material [Zhang and Ostrovski, 2002], in this work we used the procedure for the modification of the ferrous/ferric ratio in the starting powders. The pre-oxidation temperatures were selected based on the results of thermogravimetric analysis of the as-received powder (**S2**). During the pre-oxidation procedure, the powders were placed in a larger alumina crucible and heated to the targeted temperature in a chamber furnace in an air atmosphere with a heating/cooling rate of 10°C/min.

2.2. Synthesis of the compacts for thermoelectric applications

The starting powders (the as-received powder and the pre-oxidized powders) were sintered into dense compacts using two different approaches. For conventional sintering (CS), the powders were

uniaxially pressed into cylindrical pellets under 150 MPa. The pressed compacts were placed in an alumina crucible and sintered in a tube furnace in a protective atmosphere (Ar flow) at 1200°C for 5h with a heating/cooling rate of 10°C/min. Cylindrical pellets with two dimensions (diameter x height; ϕ x h) were prepared; the 8 mm x 3 mm pellets were used for structural and microstructural analyses, and measurements of absolute thermoelectric parameters, whereas the 10 mm x 10 mm pellets were used for measurements of actual thermoelectric response over a wide range of temperature gradients. For the second sintering procedure, we used an SPS furnace (FAST, Dr. Sinter FAST515-S, Sumimoto FAST Syntex Ltd., Japan). The powders were placed in a cylindrically shaped graphite die with a 10 mm diameter and pressed with 50 MPa. SPS sintering was performed in Ar atmosphere under 150 MPa pressure and with a heating rate of 100°C/min to the final temperature of 1100°C, dwell time was 5 minutes. With SPS we also prepared compacts with two dimensions: smaller ones were prepared from 0.5 g of the powders and were used for structural and microstructural characterization, whereas the larger ones were prepared from 1.5 g of the powders and were used for measurements of thermoelectric properties.

2.3. Characterization methods

Phase composition of the samples was analyzed by X-ray powder diffraction (XRD; Bruker AXS D4 Endeavor, Germany). The diffraction patterns were recorded in the angular range 10-80° 2Θ with 0.04° step size and 3s/step. The data were analyzed by X'Pert High Score Plus diffraction software. The valence state and local environment of iron in different phases in the samples were analyzed using Mössbauer spectroscopy (MS; Wissel Mössbauer spectrometer). For each measurement, we prepared around 70 mg of powder (starting powders and crushed sintered pellets) mixed with BN (boron nitride) powder. The Mössbauer spectra were recorded at room temperature using a constant acceleration Wissel spectrometer, in transmission mode with Co-57 source in Rh

matrix. Velocity calibration was performed using a thin α-Fe foil. The isomer shifts are expressed relative to α-Fe at room temperature. The spectra were fitted with the analysis code RECOIL [Lagarec and Rancourt, 1998] using Lorentzian line shape and the following parameters were refined: isomer shift (δ), quadrupole splitting (Δ), quadrupole shift (ε), magnetic hyperfine field (B_{hf}), signal line width (Γ) and relative area of the peaks (S). Microstructural analyses of the polished cross-sections of the samples were performed using scanning electron microscopy (SEM; JSM 7600F, JEOL, Japan) operated at 15 kV and equipped with energy dispersive X-ray spectrometer (EDXS; INCA Oxford 350, Oxford Instruments, UK) for the determination of chemical composition (interaction volume in the range of μm^3). Absolute density (ρ_{abs}) of the sintered compacts was measured using Densitec (Metar Sa, Rossens, Switzerland). The measurement is based on Archimedes principle, where the mass of the sample is measured in air and in oil. Relative density (ρ_{rel}) of the samples was calculated relative to the theoretical density of pseudobrookite (ρ_{Psb}= 4.4416 g/cm^3). Thermoelectric properties of the sintered compacts were determined by two methods. Absolute values of the electrical resistivity (ρ) and Seebeck coefficient (S) were measured simultaneously in the temperature range from 300 K up to 800 K using an ULVAC-ZEM3 instrument under partial helium pressure. The measurements were performed from 2 × 3 × 10 mm^3 pieces cut from the sintered pellets. The thermal conductivity (κ) was determined as the product of the geometrical density, the thermal diffusivity (Netzsch LFA457), and the theoretical heat capacity using the Dulong–Petit approximation. The lattice contribution to the thermal conductivity (κ_L) was determined by subtracting the estimated electronic component (κ_e) from the measured total thermal conductivity, κ. The electronic contribution, κ_e, was derived from the Wiedemann-Franz law, $\kappa_e = L\sigma T$, where the Lorenz number, L, was approximated from the Seebeck coefficient using the simplified expression L = 1.5 + exp(-|S|/116). Note that ρ, S and κ

were measured in the direction perpendicular to the SPS pressure direction. Thermoelectric parameters of the sintered pellets, *i.e.* the Seebeck coefficient (S), electrical conductivity (σ), and total thermal conductivity (κ) were also simultaneously measured in dependence on the temperature gradient in the temperature range from 40 °C to 450-500 °C in vacuum (10^{-2}-10^{-3} Pa) using a custom-built Z-meter based on the "large-delta-T" principle. The results of these measurements are values in a given temperature gradient between the hot and the cold side of the sample, which thus reflect the actual thermoelectric response of the material in conditions of application.

3. Results and discussion

3.1. Characterization of the starting powders

The Fe-containing phases in the starting powders (the as-received powder and the pre-oxidized powders) were analyzed by Mössbauer spectroscopy (MS). The results are shown in **Figure 2** and the refined Mössbauer parameters are given in **Table S2**. The as-received powder is altered ilmenite [Gibb et al., 1969] which contains only about half of iron in the ferrous state. Most of the Fe^{2+} is in the form of ilmenite ($FeTiO_3$, Ilm) with octahedrally coordinated Fe atoms, a minor amount of Fe^{2+} is in ulvöspinel (Fe_2TiO_4; Usp), where Fe atoms are tetrahedrally and octahedrally coordinated [Ono et al., 1968]. The remaining Fe is in the trivalent form (Fe^{3+}), mainly as pseudorutile ($Fe_2Ti_3O_9$; Prt), which is a common alteration product of ilmenite (Mücke and Chaudhuri, 1991). Some Fe^{3+} is also bound to hematite (Fe_2O_3; Hem).

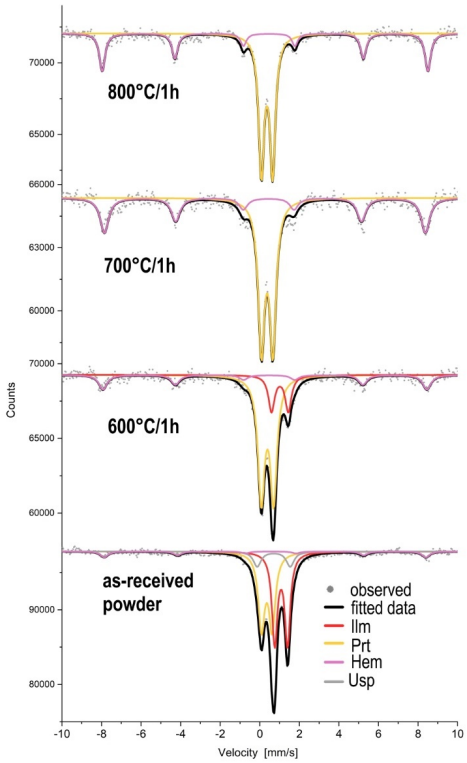

Figure 2: Mössbauer spectra of the starting powders, the as-received powder and the powders after pre-oxidation at different temperatures for 1h in air atmosphere.

After pre-oxidation of the as-received powder at 600 °C for 1 hour, the powder contains significantly less ferrous iron, only as ilmenite. The amounts of Fe^{3+} phases (Prt and Hem) increase after oxidation at 600°C and after pre-oxidation at 700°C and 800°C, the samples contain only Fe^{3+} as Prt and Hem. The result indicates that oxidation of iron is completed after 1 hour at 700°C.

XRD was used to detect the non-ferrous phases in the samples (Figure 3). The XRD pattern of the as-received powder is characterized by fairly sharp peaks, which belong to ilmenite, pseudorutile, and hematite. The presence of other phases (e.g. ulvöspinel, which was detected by MS) was below the detection limit of XRD. After pre-oxidation treatments between 600 and 800°C, the reflections of ilmenite decrease, while those of pseudorutile increase and become wider indicating increasing crystallization of pseudorutile ($Fe_2Ti_3O_9$; $3TiO_2{\cdot}Fe_2O_3$) composed of finely intergrown Fe_2O_3 and TiO_2. In addition, increasing peaks from hematite and rutile that form by progressive oxidation of ilmenite are also detected.

Commenté [ND1]: Shortened paragraph

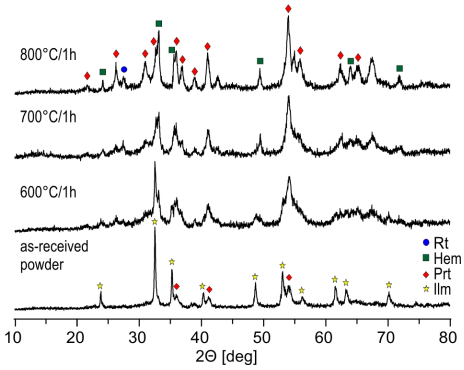

Figure 3: XRD patterns of the as-received powder and powders pre-oxidized at different temperatures.

The results of MS and XRD analyses of the starting powders suggest that ilmenite grains in the as-received powder start to oxidize already below 600°C and partially transform to rutile and hematite and partially to pseudorutile [Xiao et al., 2013; Cheng et al., 2021] via following reactions:

$$2\ FeTiO_3 + ½\ O_2 \rightarrow Fe_2O_3 + 2TiO_2 \quad (1)$$

$$12\ FeTiO_3 + 3\ O_2 \rightarrow 4\ Fe_2Ti_3O_9 + 2Fe_2O_3 \qquad (2)$$

Polished cross-sections of the as-received and pre-oxidized powders are shown in Figure 4.

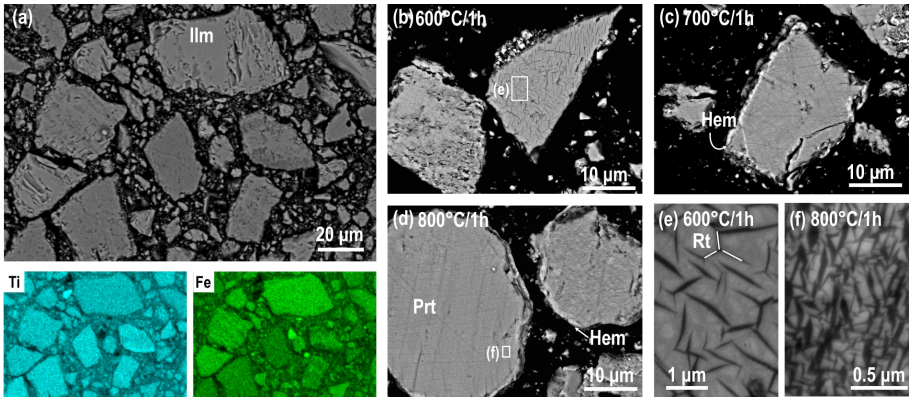

Figure 4: **(a)** As-received powder contains sharp-edged grains with variable sizes, and different Fe:Ti ratios as revealed by EDS mapping. **(b-d)** Particles after pre-oxidation at different temperatures. Ilmenite grains with different degree of crystallinity gradually recrystallize to Rt-Hem intergrowths with **(e)** coarser or finer **(f)** crystallites, the latter are characteristic for Prt.

Commenté [ND2]: Shortened

The as-received powder (Figure 4a) is composed of particles with sharp edges as a result of milling. The diameter of the particles ranges from around a micron to ~80 µm (the results of particle size analyses are shown in Figure S2). EDS mapping revealed that particles with different Fe:Ti ratios are present in the sample. Based on the Fe:Ti ratio and texture, we identified ilmenite (Fe:Ti = 1:1), pseudorutile (Fe:Ti = 2:3) and leucoxene with even lower Fe:Ti ratio, which is a result of Fe leaching during continuous alteration of the sands in placer deposits [Mücke and Bhadra

Chaudhuri, 1991]. The ilmenite and pseudorutile particles are typically homogenous, dense, and without larger rutile needles, whereas the leucoxene particles are porous due to the leaching of iron during hydrothermal alteration processes. EDS analysis of the Fe-Ti phases has revealed the presence of up to 1-2 at% (relative to all cations) of Mn, Mg and/or Al in all Fe-Ti oxides. The presence of these elements in natural ilmenite is common; the divalent cations (e.g. Mn, Mg) substitute in the Fe^{2+} sites, whereas the trivalent cations (e.g. Al) most likely occupy the Ti^{4+} sites, which requires charge compensation through the formation of Fe interstitials of O vacancies [Kuganathan et al., 2019]. SEM analyses also revealed the presence of accessory minerals like zircon, monazite, quartz and alumosilicates; however, these particles were small and fairly rare. Some examples are shown in **Figure S3**.

After pre-oxidation at different temperatures, the size and shape of the particles remain similar (**Fig. 4b-d)**, however, most of the grains contain oriented rutile exsolutions as a result of topotaxial recrystallization during oxidation of ilmenite [Rečnik et al., 2015; Stanković et al., 2016]. In addition, these grains are characterized by a thin layer of hematite on the surface as a result of Fe^{3+} out-diffusion during the process. The pre-oxidized powders contain grains with different density and size of the rutile lamellae. The transformation depends on the size and crystallinity of the starting grains; the larger and more compact grains oxidize slower [Rečnik et al., 2015; Stanković et al., 2016] in comparison to smaller grains [Fu et al., 2010] and hence, the larger ilmenite particles transform to grains with larger rutile lamellae (**Fig. 4e, left**). These lamellae are well resolved by SEM and are also detected by XRD as rutile phase. On the other hand, altered grains with higher degree of porosity transform to finer (nanoscale) oriented rutile exsolutions (**Fig. 4e, right**), which are detected as pseudorutile by XRD.

The as-received powder and the pre-oxidized powders with different Fe^{2+}: Fe^{3+} ratios were used as the starting powders for the synthesis of dense Fe-Ti-oxide compacts using conventional sintering (1200°C/5h) and spark plasma sintering (1100°C/5min) in protective Ar atmosphere.

3.2. Structural and microstructural characterization of the sintered compacts

Mössbauer spectra of the compacts prepared from different starting powders after conventional sintering and SPS are shown in **Figure 5** and the calculated Mössbauer parameters are given in **Table 2**. The sintered compacts prepared from **as-received powder** have similar compositions after both sintering procedures (CS and SPS). The only Fe^{2+}-containing product is ferropseudobrookite [Guo et al., 1999], whereas the presence of some ilmenite indicates that it remained partially unreacted during the sintering in Ar. Both ferric oxides from the starting powder, pseudorutile and hematite, completely transformed into pseudobrookite. The presence of ferropseudobrookite is observed also in the samples prepared from the **powder pre-oxidized at 600°C**, which contained some residual ilmenite. Interestingly, conventionally sintered compacts prepared from the **powders pre-oxidized at 700 and 800°C** contain some ferropseudobrookite even though the powders were fully oxidized in the pre-oxidation step (**Table 1**). This suggests that some Fe^{3+} from Fe_2TiO_5 was reduced back to Fe^{2+} during the 5 h sintering at 1200°C in argon. The reduction of iron did not occur in the samples sintered by SPS due to the lower sintering temperature (1100°C) and significantly shorter sintering time of only 5 minutes. The only Fe-phase in these samples is pseudobrookite.

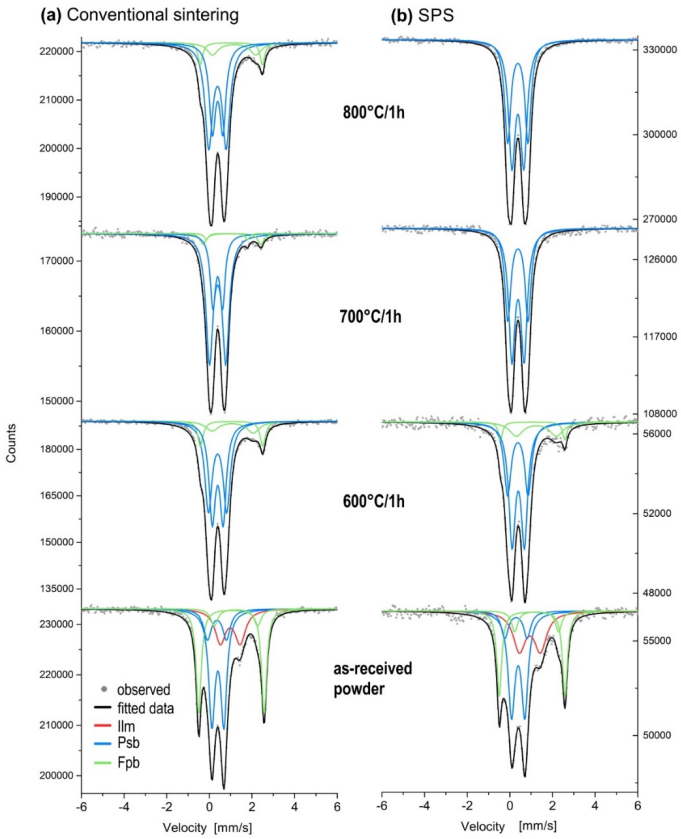

Figure 5: Mössbauer spectra of the different starting powders (as-received and pre-oxidized) after **(a)** conventional sintering and **(b)** SPS.

The best fit for ferropseudobrookite and pseudobrookite was obtained when Fe^{2+} and Fe^{3+} were distributed to 4f and 8f surroundings in all samples. This indicates that ferropseudobrookite and

pseudobrookite have disordered crystal structures with ferrous and ferric cations residing in both structural positions along with the Ti^{4+}.

The results of XRD analyses (**Figure 6**) confirm the findings by MS that the main component of all sintered compacts are phases on the pseudobrookite-ferropseudobrookite (Psb-Fpb) tie-line. In the conventionally sintered samples, the Psb-Fpb peaks are sharp and well-defined indicating good crystallinity of the phase. On the other hand, the Psb-Fpb peaks in SPS samples are wider indicating smaller crystallites and poor crystallinity due to a combination of much faster heating/cooling rates, shorter sintering time, and application of pressure during the sintering.

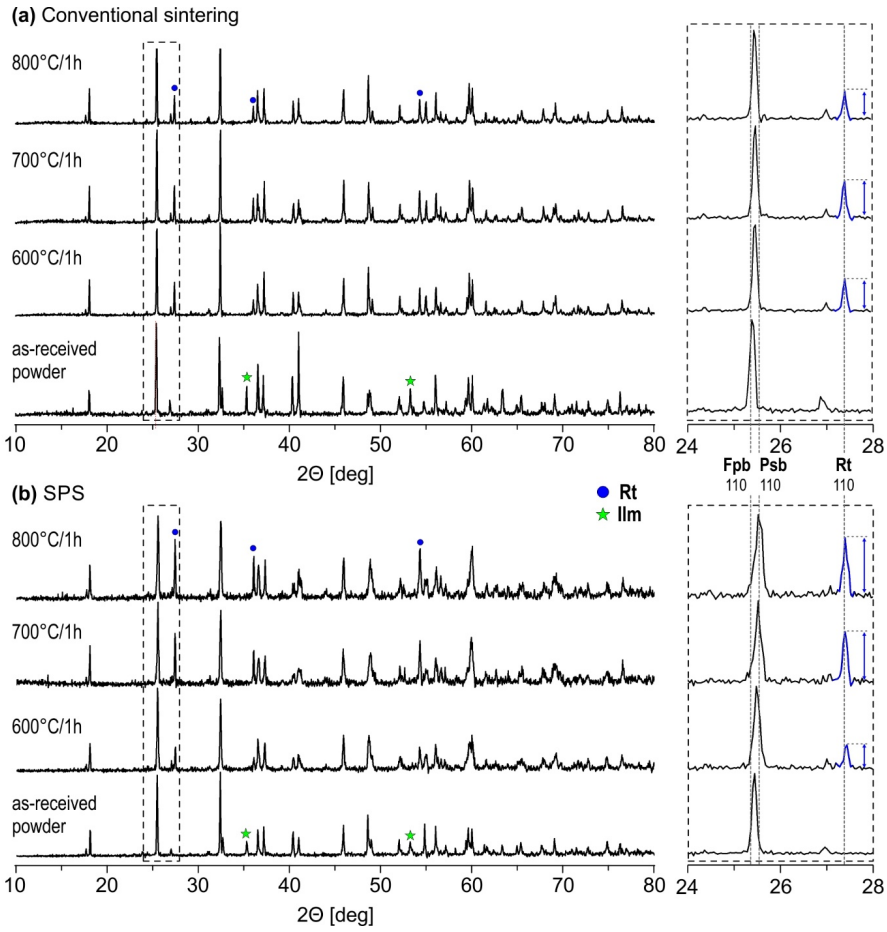

Figure 6: XRD patterns of the starting powders after **(a)** conventional sintering and **(b)** SPS.

The samples prepared from the as-received powder via both sintering procedures (CS and SPS) contain only phases on the Psb-Fpb tie-line and some ilmenite. No rutile was detected in these samples. On the other hand, all samples prepared from pre-oxidized powders contain rutile that

formed during the pre-oxidation stage. The intensity of rutile reflections in the CS samples is similar in all samples prepared from powders pre-oxidized at different temperatures, whereas the intensity of rutile reflections in compacts prepared by SPS increases with pre-oxidation temperature (see the detail on the right side of Figure 6). This suggests that, during conventional sintering, some rutile reacted with Psb, triggering a reduction of Fe^{3+} to Fe^{2+} and the formation of Fpb according to the following reaction:

$$Fe_2TiO_5 + 3TiO_2 \rightarrow 2FeTi_2O_5 + ½\ O_2 \qquad (3)$$

The results of MS and XRD analyses have shown that the samples prepared by conventional sintering and SPS from the same starting powders have comparable phase composition; however, microstructural analyses (Figure 7) reveal that the samples prepared by those different processing routes have different grain sizes, densities (Table 3), and distribution of phases.

Table 3: Absolute and relative densities of samples prepared from different starting powders after **(a)** conventional sintering and **(b)** SPS.

(a) Conventional sintering

Sample	Measured density [g/cm^3]	Relative density [%]
as-received powder	4.071	89.6
600°C/1h	3.648	83.0
700°C/1h	3.717	84.0
800°C/1h	3.796	86.2

(b) SPS

Sample	Measured density [g/cm^3]	Relative density [%]
as-received powder	4.238	95.1
600°C/1h	4.244	96.8
700°C/1h	4.263	96.8
800°C/1h	4.274	97.1

The microstructures of the samples after conventional sintering are shown in **Figure 7a**. The sample prepared from **as-received powder** has the highest density (89.6 %) and the largest grain size (~ 10 - 50 microns) among the conventionally sintered samples. Areas with different gray levels in backscattered images indicate areas with different Fe:Ti ratios. According to MS and XRD, this sample contains mainly pseudobrookite, ferropseudobrookite, and some ilmenite. These phases have theoretical Fe:Ti ratios of 2, 0.5, and 1, respectively. SEM/EDS analyses have shown that the darker regions, which are prevailing in the sample, have a fairly constant Fe:Ti ratio of around 0.8 (Fpb:Psb ~ 60:40), whereas the brighter areas contain more Fe and have the Fe:Ti ratio of around 1.5 (Fpb:Psb ~ 10:90). This indicates that Psb and Fpb form two solid solutions with stable Fe^{2+}:Fe^{3+} ratios. Some grains with an even higher amount of Fe were found, whereas grains with a Fe:Ti ratio of 1 (as expected for ilmenite) were not found even though the presence of ilmenite was indicated by MS and XRD. Microstructural characteristics of the sample suggest that the starting powder, composed of up to 40 μm large particles of pseudorutile, ilmenite, and some ulvöspinel and hematite locally recrystallized to grains with Psb-Fpb composition, and the processes are governed by slow diffusion.

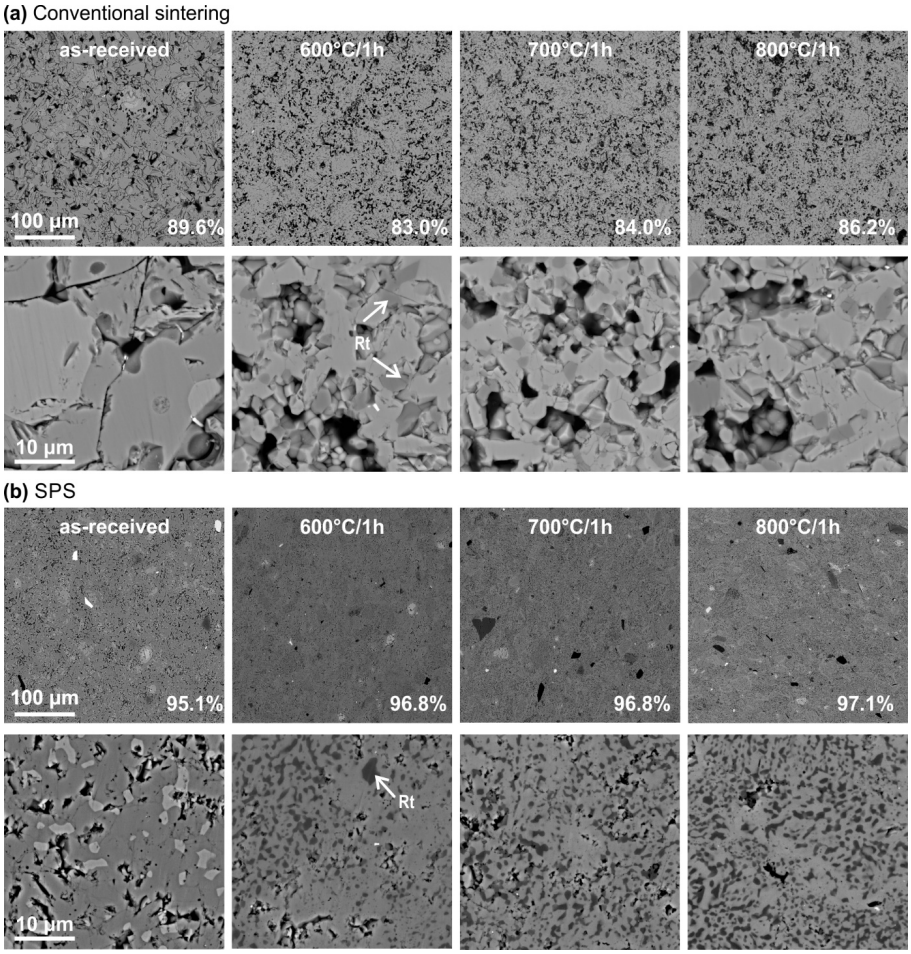

Figure 7: Microstructures of the as-received powder and pre-oxidized samples after **(a)** conventional sintering (1200°C/5h) and **(b)** SPS (1100°C/5min). *Higher magnification micrographs are presented in the second row.*

Samples prepared from **pre-oxidized powders** have higher porosity, relative density between 83 and 86%, and grain size below 10 microns. In these samples, iron is prevalently in the Fe^{3+} form

and hence the matrix phase grains have a more uniform Fe:Ti ratio, which is most likely a solid solution between pseudobrookite and ferropseudobrookite. Typical for these samples is the presence of intergranular rutile grains, which formed by aggregation of rutile lamellae that formed in the ilmenite grains during the pre-oxidation. During high-temperature sintering, the rutile lamellae inhibited the diffusion processes and therefore, the matrix (Psb-Fpb) grains remained smaller in comparison to the sample prepared from as-received powder without the rutile lamellae.

Samples sintered by **SPS** (Figure 7b) have smaller grain sizes and higher relative densities, above 95%, in comparison to conventionally sintered samples. The microstructural characteristics are a consequence of the fast heating rate under the applied pressure. Similar to the CS samples, the SPS sample prepared from the **as-received powder** has the largest grain size, and also here, areas with two different gray levels (Z-contrast in back-scattered images) are observed. The majority of the sample has Fe:Ti ratio of around 0.8 (darker regions, mostly Fpb), whereas the brighter regions have Fe:Ti ratio of around 1.5 (brighter regions; mostly Psb). This confirms that two solid solutions with stable composition are formed during the sintering by local recrystallization.

The samples prepared from **pre-oxidized powders** are composed of pseudobrookite matrix with micron and sub-micron rutile inclusions that occur as intra- and inter-granular particles. Regions with different concentrations of rutile needles are observed depending on the composition of the particle in the starting powder, e.g. pseudorutile or ilmenite with rutile needles, confirming that densification of the sample includes only local recrystallization.

3.3. Measurements of thermoelectric properties

The electrical and thermal transport properties of the three series of samples, measured between 300 K and 800 K, are given in Figure 8. Both samples, sintered conventionally at 1200°C or by

SPS at 1100 °C from as-received powders, exhibit an *n*-type behavior with rather low absolute values of the Seebeck coefficient of respectively 27 and 52 μV K^{-1} at room temperature (**Figure 8a**). It increases linearly with temperature up to around 85-90 μV K^{-1} at 800 K. Such a low magnitude of $|S|$ and its linear increase with temperature is in agreement with the mixed valence Fe^{2+}/Fe^{3+} observed in those two samples (**Table 2**). Such behavior is typically observed in electron-doped TiO_2, $SrTiO_3$, and $CaMnO_3$, where mixed valence Ti^{3+}/Ti^{4+} or Mn^{3+}/Mn^{4+} promotes electron conduction [X. Liu et al., 2021; J. Wang et al., 2017; Lu et al., 2016; Srivastava et al., 2018; Kanas et al., 2022]. Surprisingly, the electrical resistivity (**Figure 8b**) decreases with temperature for both samples, which suggests the carrier concentration remains relatively low and/or microstructural features, such as the existence of many interfaces, also govern the electrical conduction.

The samples, **sintered by SPS** from powders pre-oxidized at 600°C, 700°C or 800°C, have larger absolute values of the Seebeck coefficient, which increase with the annealing temperature from 250 μV K^{-1} for the 600°C-SPS sample to 400 μV K^{-1} for the 700°C-SPS sample at 300 K and 616 μV K^{-1} at 500 K for the 800°C-SPS sample. This evolution can be directly linked to the decrease of Fe^{2+} content from 52% in the raw sample to 2% in the 600°C-SPS sample and 0% in the 700°C-SPS and 800°C-SPS samples (**Table 2b**). The largest amount of rutile phase in those two samples can also affect the Seebeck coefficient. Note that the electrical resistivity in this series increases with the annealing temperature, in agreement with the increase in the absolute value of $|S|$.

The samples, **sintered conventionally** at 1200°C, do not exhibit significant and regular variations of the Seebeck coefficient with the annealing temperature. All $|S|$ values range between 325 and 375 μV K^{-1} at 450 K. This trend is correlated with the existence of Fe^{2+}/Fe^{3+} mixed valence in those samples (**Table 2**), due to the reduction induced by the high-temperature sintering. The magnitude of the electrical resistivity does not vary significantly with the annealing temperature which is in

good agreement with the Seebeck coefficient values. Note that the largest porosity in this series of samples does not significantly influence the magnitude of the electrical resistivity compared with the two other series of samples.

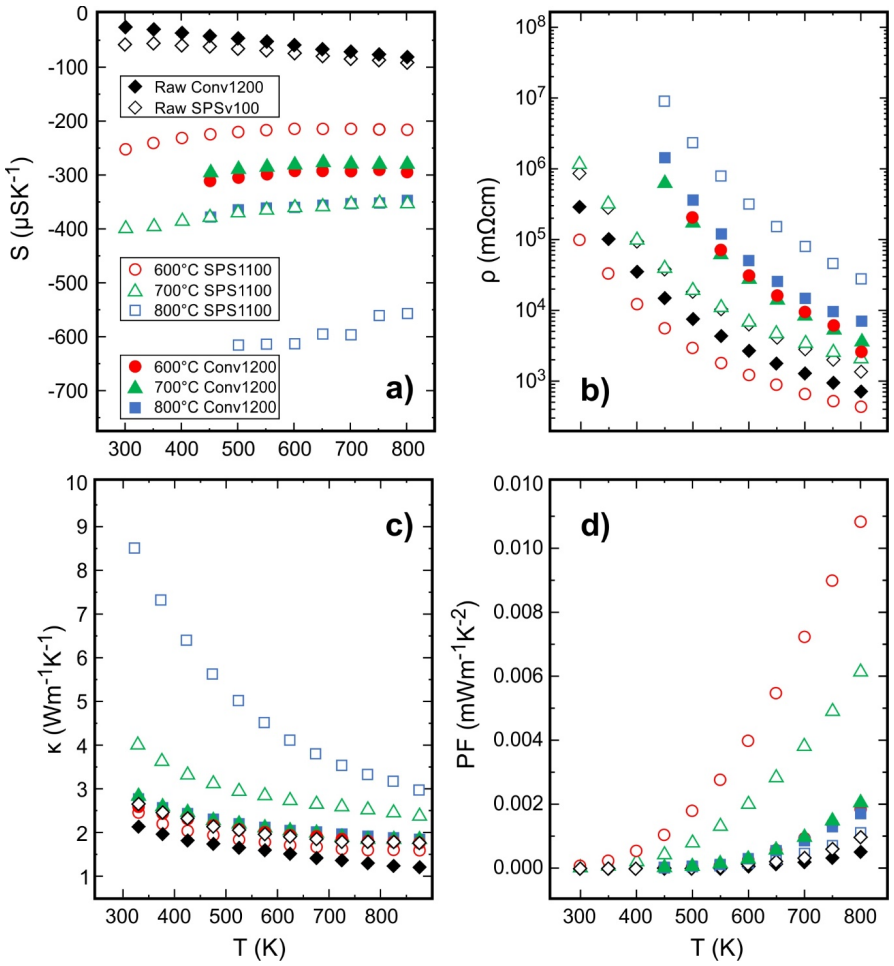

Figure 8: Thermoelectric properties of untreated and pre-oxidized powders after conventional sintering and SPS. **(a)** Seebeck coefficient, **(b)** electrical resistivity, **(c)** thermal conductivity, and **(d)** power factor, as a function of temperature.

The temperature dependence of the **thermal conductivity**, displayed in Figure 8c, indicates that all the samples prepared from as-received powders exhibit similar values in the full temperature range. Those values are relatively low for oxide compounds, ranging between 2 and 3 W m^{-1} K^{-1}. Surprisingly, the sample sintered by SPS from powders annealed at 700°C or 800°C presents large values, especially for the latter sample. This behavior seems related to the increase of rutile content in those samples combined with high relative densities.

The **power factor (PF) values**, shown in Figure 8d, are extremely low, reaching a maximum value of 0.011 mW m^{-1} K^{-2} at 800 K for the sample sintered by SPS at 1100°C from powders annealed at 600°C. The low values are mainly explained by the high electrical resistivity of the present samples. Despite the low Seebeck coefficient in the raw sample series, the presence of different phases probably decreases the electron mobility. Unfortunately, due to the existence of different phases, many interfaces, and Fe^{2+}/Fe^{3+} mixed valence, attempts to measure the carrier concentration were unsuccessful. Strategies for improvement of electrical properties include the adjustment of Fe:Ti ratio in the starting powders by the addition of extra hematite (Fe_2O_3) to trigger preferential formation of pseudobrookite (Fe_2TiO_5; Fe:Ti=2) and prevent the formation of rutile phase. In addition, the electrical conductivity may be improved by Nb doping es shown by experimental study [Chen et al., 2017] and ab-initio calculations [Mohammadi and Pakizeh, 2022].

The **Seebeck coefficient and the thermal conductivity** of the compacts were also measured by the Z-meter in the temperature gradients across the sample from 27 K to 390 K for the temperature

on the hot side of the sample from about 45°C to 450°C, respectively. The electrical resistivity of all the samples was above about 1 Ωm and thus outside the measuring range of the system; hence it was not determined by the Z-meter. The values determined by the use of the Z-meter show a similar trend in the Seebeck coefficient for SPS and conventionally sintered samples prepared from untreated and pre-oxidized powders than the values obtained by the ZEM-3, but they are noticeably lower due to the large ΔT across the sample during the measurement. Nevertheless, the largest values of the Seebeck coefficient are close to 300 μV/K. Also, the Seebeck coefficient is quite constant regarding the ΔT in most of the samples (**S5a**).

The thermal conductivities measured by the Z-meter are shown in supporting materials (**S5b**). As they were determined in a large ΔT regime, they are lower as compared to the values determined by the use of the laser flash method, ranging from about 2.2W/mK to about 0.7W/mK. It is also worth mentioning that thermal conductivity is rather constant in all the samples regardless of the temperature gradient across the sample. The fact that quite high Seebeck coefficient and quite low thermal conductivity of the samples are constant in a relatively broad range of temperature gradients from about 30K to even about 400K (i.e. temperatures of the hot side from 45°C to 450°C, respectively), is encouraging for the application of these materials. The differences between the results obtained by ZEM-3 and the Z-meter can be explained by the complexity of the samples due to their inhomogeneous composition and microstructure, which is likely more expressed in the case of larger samples measured by the Z-meter under large ΔT than in the case of much smaller samples measured by ZEM-3 at small ΔT and thus affects the obtained results.

4. Conclusions

In this work, we used natural Fe-Ti-rich heavy mineral sand as a raw material for the preparation of ceramics for thermoelectric applications. The phase composition and microstructural properties of the sintered compacts and the related thermoelectric properties depend on the starting Fe:Ti ratio, the application of the pre-oxidation procedure of the as-received powder, and the sintering process (conventional sintering or SPS). All samples exhibit relatively low thermal conductivity for oxides, but the ZT values of all samples are very low due to the low PF values. The best properties were obtained for the SPS sintered powder that was pre-oxidized at 600 °C. Further investigations are required to optimize the electrical conduction by balancing the starting Fe:Ti ratio to avoid the formation of rutile and appropriate doping strategies. The correlation between Mössbauer spectroscopy and electrical transport properties data indicates that the mixed valence Fe^{2+}/Fe^{3+} is the key parameter to generate optimized thermoelectric performances. Nevertheless, the measured values of thermoelectric parameters obtained on samples prepared from natural powders are comparable to those obtained on samples prepared from pure (>99%) starting chemicals [Chen et al., 2017; Chen et al., 2018]. The results of this study suggest that natural Fe-Ti-rich heavy sands, which represent abundant, nontoxic, and low-cost raw materials, are potentially interesting for the preparation of ceramics for thermoelectric application after some additional improvements.

Acknowledgements

The authors gratefully acknowledge financial support by the Slovenian Research Agency under the Project No. J1-9177, Programme P2-0091, and Programme P1-0112. EG and SB thanks Campus France for financial support (PROTEUS 44203UB**).**

References

M. Araiz, Á. Casi, L. Catalán, Á. Martínez, D. Astrain, Prospects of waste-heat recovery from a real industry using thermoelectric generators: Economic and power output analysis, Energy Conversion and Management 205 (2020) 112376, https://doi.org/10.1016/j.enconman.2019.112376.

C. Chen, F. Giovannelli, F. Delorme, Thermoelectric properties of $Fe_{2-x}Ti_{1+x}O_5$ solid solutions: Influence of microcracking and Nb substitution, Ceramics International 44 (2018) 21794-21799, https://doi.org/10.1016/j.ceramint.2018.08.282.

C. Chen, F. Giovannelli, J-R. Duclère, F. Delorme, Thermoelectric properties of $Fe_2(Ti_{1-x}Nb_x)O_5$ pseudobrookite ceramics with low thermal conductivity, Journal of the European Ceramic Society 37 (2017) 4681-4685, https://doi.org/10.1016/j.jeurceramsoc.2017.06.027.

C. Chen, B. R. Müller, O. I. Lebedev, F. Giovannelli, G. Bruno, F. Delorme, Effects of impurities on the stability of the low thermal conductivity in Fe_2TiO_5 ceramics, Materials Characterization 149, (2019) 111-117, https://doi.org/10.1016/j.matchar.2019.01.021.

G. Cheng, Z. Gao, S. Yang, H. Yang, X. Xue, Microstructure and chemical transformation of natural ilmenite during isothermal roasting process in air atmosphere, Minerals 11 (2021) 137, https://doi.org/10.3390/min11020137.

X. Fu, Y. Wang, F. Wei, Phase Transitions and Reaction Mechanism of Ilmenite Oxidation, Metallurgical and Materials Transactions A, 41 (2010) 1338-1348, https://doi.org/10.1007/s11661-010-0173-y.

T.C. Gibb, N.N. Greenwood, W. Twist, The Mössbauer Spectra of Natural Ilmenites, Journal of Inorganic and Nuclear Chemistry 31 (1969) 947-954, https://doi.org/10.1016/0022-1902(69)80142-9.

F. Giovannelli, C. Chen, P. Díaz-Chao, E. Guilmeau, F. Delorme, Thermal conductivity and stability of Al-doped ZnO nanostructured ceramics, Journal of the European Ceramic Society 38 (2018) 5015-5020, https://doi.org/10.1016/j.jeurceramsoc.2018.07.032.

E. Guilmeau, P. Díaz-Chao, O. I. Lebedev, A. Rečnik, M. C. Schäfer, F. Delorme, F. Giovannelli, M. Košir, S. Bernik, Inversion Boundaries and Phonon Scattering in Ga:ZnO Thermoelectric Compounds, Inorganic Chemistry 56 (2017) 480-487, https://doi.org/10.1021/acs.inorgchem.6b02354.

W. Q. Guo, S. Malus, D. H. Ryan, Z. Altounian, Crystal structure and cation distributions in the $FeTi_2O_5$-Fe_2TiO_5 solid solution series, Journal of Physics: Condensed Matter 11 (1999) 6337-6346, https://doi.org/10.1088/0953-8984/11/33/304.

S.K. Gupta, V. Rajakumar, P. Grieveson, Phase transformations during heating of ilmenite concentrates, Metallurgical and Materials Transactions B 22 (1991) 711–716. https://doi.org/10.1007/BF02679027.

W. Jiangtao, Y. Liangliang, Ma.Zhe, S. Peishuai, Z. Mingliang, M. Jing, Y. Fuhua, W. Xiaodong, Review of current high-ZT thermoelectric materials, Journal of Materials Science 5 (2020) 12642–12704, https://doi.org/10.1007/s10853-020-04949-0.

G. Jones. "Mineral Sands: an Overview of the Industry" Iluka (unpublished), 2009, 26 pages. (link)

N. Kanas, B. A. D. Williamson, F. Steinbach, R. Hinterding, M.-A. Einarsrud, S. M. Selbach, A, Feldhoff, K, Wiik, Tuning the Thermoelectric Performance of CaMnO3-Based Ceramics by Controlled Exsolution and Microstructuring, ACS Applied Energy Materials 10 (2022) 12396-12407, https://doi.org/10.1021/acsaem.2c02012.

M. Košir, M. Čeh, C. W. Ow-Yang, E. Guilmeau, S.Bernik, Structural features and thermoelectric properties of Al-doped $(ZnO)_5In_2O_3$ homologous phases, Journal of the European Ceramic Society, https://doi.org/10.1111/jace.14878.

N. Kuganathan, R. Srikaran, P. C. M. Fossati, A. Chroneos, Theoretical Modeling of Defects, Dopants, and Diffusion in the Mineral Ilmenite, Minerals 9 (2019) 1-13, https://doi.org/10.3390/min9100610.

J.-B. Labégorre, O. I. Lebedev, C. Bourgès, A. Rečnik, M. Košir, S. Bernik, A. Maignan, T. Le Mercier, L. Pautrot-d'Alençon, E. Guilmeau, Phonon Scattering and Electron Doping by 2D Structural Defects in In/ZnO, ACS Applied Materials & Interfaces 10 (2018) 6415-6423, https://doi.org/10.1021/acsami.7b19489.

K. Lagarec, D.G. Rancourt. Recoil − Mössbauer spectral analysis software for Windows. Department of Physics, University of Ottawa, Ottawa, ON, Canada (1998) version 1.0, pp. 43.

K. H. Lee, S. W. Kim, H. Ohta, K. Koumoto, Ruddlesden-Popper phases as thermoelectric oxides: Nb-doped $SrO(SrTiO_3)_n$ (n=1,2), Journal of Applied Physics 100 (2006) 063717. https://doi.org/10.1063/1.2349559.

Y.-H. Lin, J. Lan, C. Nan, Oxide thermoelectric materials: From basic Principles to Applications, Wiley (2019) pp. 270.

D.H. Lindsley, Experimental studies of oxide minerals. Reviews in Mineralogy and Geochemistry 25 (1991) 69–106, https://doi.org/10.1515/9781501508684-006.

X. Liu, D. Kepaptsoglou, Z. Gao, A. Thomas, K. Maji, E. Guilmeau, F. Azough, Q. M. Ramasse, R. Freer, Controlling the Thermoelectric Properties of Nb-Doped TiO_2 Ceramics through Engineering Defect Structures. ACS Applied Materials & Interfaces 13 (2021) 57326-57340, https://doi.org/10.1021/acsami.1c18236.

Z. Lu, H. Zhang, W. Lei, D. C. Sinclair, I. M. Reaney, High-Figure-of-Merit Thermoelectric La-Doped A-Site-Deficient $SrTiO_3$ Ceramics, Chemistry of Materials 28 (2016) 925-935, https://doi.org/10.1021/acs.chemmater.5b04616.

A. C. Masset, C. Michel, A. Maignan, M. Hervieu, O. Toulemonde, F. Studer, and B. Raveau, J. Hejtmanek, Misfit-layered cobaltite with an anisotropic giant magnetoresistance: $Ca_3Co_4O_9$, Physical Review B 62 (2000) 166-175, https://doi.org/10.1103/PhysRevB.62.166.

A. Mücke, J.N. Bhadra Chaudhuri, The continuous alteration of ilmenite through pseudorutile to leucoxene, Ore Geology Reviews 6 (1991) 25-44, https://doi.org/10.1016/0169-1368(91)90030-B.

H. Ohta, S. Kim, Y. Mune, T. Mizoguchi, K. Nomura, S. Ohta, T. Nomura, Y. Nakanishi, Y. Ikuhara, M. Hirano, H. Hosono, K. Koumoto, Giant thermoelectric Seebeck coefficient of a two-dimensional electron gas in $SrTiO_3$, Nature Materials 6 (2007) 129-34, https://doi.org/10.1038/nmat1821.

M. Ohtaki, T. Tsubota, K. Eguchi, and H. Arai, High-temperature thermoelectric properties of $(Zn_{1-x}Al_x)O$, Journal of Applied Physics 79 (1996) 1816-1818, https://doi.org/10.1063/1.360976.

K. Ôno, L. Chandler, A. Ito, Mössbauer Study of the Ulvöspinel, Fe_2TiO_4. Journal of the Physical Society of Japan 25 (1968) 174−176, https://doi.org/10.1143/JPSJ.25.174.

E. Pakizeh, M. Mohammadi, Structural, electronic, magnetic and thermoelectric properties of pseudobrookite-type $Fe_{2-x}Ti_{1+x}O_5$ (x = 0, 0.5 and 1) compounds: DFT + U approaches" Journal of Physics and Chemistry of Solids 149, 2021, 109802. https://doi.org/10.1016/j.jpcs.2020.109802.

P. Ramdohr, The ore minerals and their intergrowths, 3rd Edition (1969) Pergamon Press Ltd., London.

A. Rečnik, N. Stanković, N. Daneu, Topotaxial reactions during the genesis of oriented rutile/hematite intergrowths from Mwinilunga (Zambia), Contributions to Mineralogy and Petrology 169 (2015) 19, https://doi.org/10.1007/s00410-015-1107-x.

R.G. Rejith, M. Sundararajan, Combined magnetic, electrostatic, and gravity separation techniques for recovering strategic heavy minerals from beach sands, Marine Georesources & Geotechnology 36 (2018) 959-965, https://doi.org/10.1080/1064119X.2017.1403523.

G. Ren, J. Lan, C. Zeng, Y. Liu, B. Zhan, S. Butt, Y.-H. Lin, C.-W. Nan., High Performance Oxides-Based Thermoelectric Materials" JOM 67 (2015) 211–221, https://doi.org/10.1007/s11837-014-1218-2

M. Shikano, R. Funahashi, Electrical and thermal properties of single-crystalline $(Ca_2CoO_3)_{0.7}CoO_2$ with a $Ca_3Co_4O_9$ structure, Applied Physics Letters 82 (2003) 1851-1853, https://doi.org/10.1063/1.1562337.

D. Srivastava, C. Norman, F. Azough, M. C. Schäfer, E. Guilmeau, R. Freer, Improving the thermoelectric properties of $SrTiO_3$-based ceramics with metallic inclusions, Journal of Alloys and Compounds 731 (2018) 723-730, https://doi.org/10.1016/j.jallcom.2017.10.033.

N. Stanković, A. Rečnik, N. Daneu, Topotaxial reactions during oxidation of ilmenite single crystal, Journal of Materials Science 51 (2016) 958–968, https://doi.org/10.1007/s10853-015-9425-y.

I. Terasaki, Y. Sasago, K. Uchinokura, Large Thermoelectric Power in $NaCo_2O_4$ Single Crystals, Physical Review B56 (1997) R12685-R12687, https://doi.org/10.1103/PhysRevB.56.R12685.

G. Zhang, O. Ostrovski, Effect of preoxidation and sintering on properties of ilmenite concentrates. International Journal of Mineral Processing, 64 (2002) 201-218, https://doi.org/10.1016/S0301-7516(01)00055-2.

J. Zhang, Q. Zhu, Z. Xie, C. Lei, H. Li, Morphological Changes of Panzhihua Ilmenite During Oxidation Treatment. Metallurgical and Materials Transactions B, 44 (2013) 897-905, https://doi.org/10.1007/s11663-013-9863-3.

W. Xiao, X.-G. Lu, X.-L. Zou, X.-M. Wei, W-Z. Ding, Phase transitions, micro-morphology and its oxidation mechanism in oxidation of ilmenite ($FeTiO_3$) powder. Transactions of Nonferrous Metals Society of China, 23 (2013) 2439-2445, https://doi.org/10.1016/S1003-6326(13)62752-1.

J. Wang, B.-Y. Zhang, H.-J. Kang, Y. Li, X. Yaer, J.-F. Li, Q. Tan, S. Zhang, G.-H. Fan, C.-Y. Liu, L. Miao, D. Nan, T.-M. Wang, L.-D. Zhao, Record high thermoelectric performance in bulk $SrTiO_3$ via nano-scale modulation doping, Nano Energy 35 (2017) 387-395, https://doi.org/10.1016/j.nanoen.2017.04.003.